

Prototyping method for Bragg-type atom interferometers

Brandon Benton,¹ Michael Krygier,¹ Jeffrey Heward,¹ Mark Edwards,¹ and Charles W. Clark²

¹*Department of Physics, Georgia Southern University, Statesboro, GA 30460-8031 USA*

²*Joint Quantum Institute, National Institute of Standards and Technology
and the University of Maryland, Gaithersburg, MD 20899, USA*

(Dated: November 13, 2018)

We present a method for *rapid* modeling of new Bragg ultra-cold atom interferometer (AI) designs useful for assessing the performance of such interferometers. The method simulates the overall effect on the condensate wave function in a given AI design using two separate elements. These are (1) modeling the effect of a Bragg pulse on the wave function and (2) approximating the evolution of the wave function during the intervals between the pulses. The actual sequence of these pulses and intervals is then followed to determine the approximate final wave function from which the interference pattern can be calculated. The exact evolution between pulses is assumed to be governed by the Gross-Pitaevskii (GP) equation whose solution is approximated using a Lagrangian Variational Method to facilitate rapid estimation of performance. The method presented here is an extension of an earlier one that was used to analyze the results of an experiment [J.E. Simsarian, et al., Phys. Rev. Lett. **83**, 2040 (2000)], where the phase of a Bose-Einstein condensate was measured using a Mach-Zehnder-type Bragg AI. We have developed both 1D and 3D versions of this method and we have determined their validity by comparing their predicted interference patterns with those obtained by numerical integration of the 1D GP equation and with the results of the above experiment. We find excellent agreement between the 1D interference patterns predicted by this method and those found by the GP equation. We show that we can reproduce all of the results of that experiment without recourse to an *ad hoc* velocity-kick correction needed by the earlier method, including some experimental results that the earlier model did not predict. We also found that this method provides estimates of 1D interference patterns at least four orders-of-magnitude faster than direct numerical solution of the 1D GP equation.

PACS numbers: 03.75.Dg, 67.85.Hj, 03.67.Lx, 03.75.Kk, 42.50.Gy

I. INTRODUCTION

It is possible to use ideas inspired by advances in quantum information science (QIS) to devise improved-performance matter-wave interferometers. A recent example of this has been seen in neutron interferometry where the idea of decoherence-free subspaces was used to redesign a neutron interferometer to reduce the effect of mechanical shaking on the interference contrast [1, 2]. The use of ideas from QIS to drive new neutron interferometer designs may also be possible for atom interferometers. Two promising areas of QIS where this could happen include decoherence avoidance and minimization. Interferometer applications where QIS-inspired redesigns may result in improved performance include precision navigation and metrology. This paper presents a tool for rapid assessment of new atom-interferometer designs for such applications.

Atom interferometers (AI), where laser light is applied to ultra-cold atoms, have many applications. These include quantum decoherence [3, 4], properties of Bose-Einstein condensates [5–8], precision measurement of the fine-structure constant [9, 10] and testing the charge neutrality of atoms [11]. Atom interferometers are also used in many precision measurement devices. These include gravimeters, gyroscopes, and gradiometers which all have important applications in precision navigation [12–14]. Atom interferometers also have applications in atomic physics such as atomic polarizability measurements and

Casimir-Polder potentials for atoms near surfaces [15]. More uses of atom interferometry are described in Ref. [16].

With the advent of gaseous Bose-Einstein condensates (BEC) [17–21], strong interest has developed in using AIs for precision metrology [10, 22–28]. Most of these ultra-cold atom interferometers were of the standard Mach-Zehnder design. However, some more recent precision interferometers [10] have different designs. This also suggests that advances in interferometer design may lead to significant AI performance gains.

There are many factors that can limit the performance of an AI. Some of these include mirror vibration, random initial motion of BECs at birth, stray light, external magnetic fields, and errors in the frequency or intensity of the applied laser light. Atom interferometers confined on an atom chip can have other problems related to atom loss, heating, and decoherence [29]. One of the ways in which some of these factors may be addressed is with new AI designs.

In order to pursue the program of drawing ideas from QIS to inspire new AI designs, it will be necessary to develop tools that can be used to provide *rapid* assessment of the performance of these new designs. In this work we present a method for rapid simulation of the behavior of condensates in Bragg interferometers. We assume that the evolution of the condensate between Bragg pulses is described by the Gross-Pitaevskii (GP) equation. The method approximates the evolution of the condensate

wave function by modeling the effect of individual pulses and its evolution between pulses. Thus the final condensate wave function can be found enabling the prediction of the final interference pattern. As will be seen below, our method provides reasonable estimates of AI behavior in a time that is four orders-of-magnitude faster than that needed for numerical solution of the (1D) GP equation to simulate a standard Mach-Zehnder AI. The time-savings factor for 3D simulation will be greater. Such a tool will be essential for preliminary testing of new AI designs having more pulses and longer evolution times.

In Section II we describe the standard $\pi/2$ - π - $\pi/2$ Bragg interferometer followed in Section III by a general overview of the two elements of our Bragg prototyper model and the details of the original model used in the analysis of a Bragg interferometer experiment carried out at NIST [30]. In the original model each definite-momentum cloud in the condensate wave function was represented by a single gaussian. An extra velocity “kick”, caused by the repulsion of the separating clouds after a $\pi/2$ Bragg pulse, was needed to obtain agreement with the experimental results. A study of this kick for a single pulse was conducted as a function of interaction strength of the condensate and the results are presented in Section IV. Section V presents the two-cloud version of our Bragg prototyper model for both the 1D and 3D cases. Finally, Section VI contains a summary and discussion of the possible applications of the method.

II. BRAGG ATOM INTERFEROMETER

A Bose-Einstein condensate (BEC) can be coherently split into two clouds, a fast-moving cloud and a slow-moving cloud, through the application of a Bragg pulse [31]. If the condensate is stationary when a Bragg pulse is applied to it, then the result will be two clouds, one that remains stationary and another whose momentum is $\hbar\Delta\mathbf{k} = \hbar(\mathbf{k}_1 - \mathbf{k}_2)$ where \mathbf{k}_1 (\mathbf{k}_2) is the photon momentum of the higher (lower) frequency laser beam. If the condensate is moving with this momentum when the Bragg pulse is applied, then the result is again two clouds one of which keeps its momentum while the other cloud’s momentum is reduced by $\hbar\Delta\mathbf{k}$. In either case, the net result of applying a Bragg pulse to a condensate is a fast cloud and a slow cloud. One of these clouds has the momentum of the original cloud and the momentum of the other cloud is increased (decreased) if the original cloud was slow (fast).

A Mach-Zehnder-type Bragg interferometer can be constructed by applying three Bragg pulses in the sequence $\pi/2$ - π - $\pi/2$ with variable time intervals between them [32]. This is shown in Fig. 1 where the open circle shows the initial condensate which may be released from the trap and allowed to expand for a time T_0 . The first $\pi/2$ pulse splits the condensate into a slow cloud (upper path) and a fast cloud (lower path). After a time interval T_1 the π pulse is applied which stops the fast (lower)

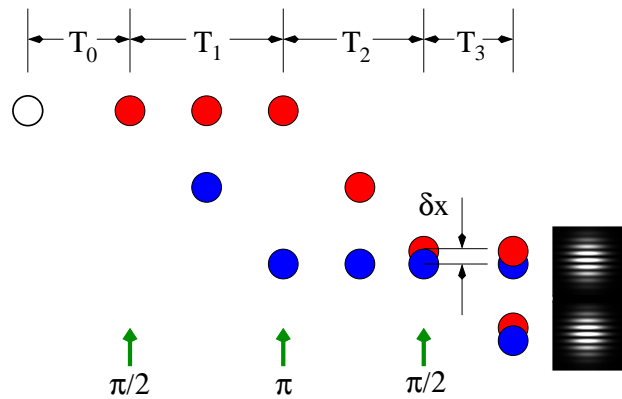


FIG. 1: (color online) This figure shows the sequence of Bragg pulses (represented by green arrows) applied to a condensate in a $\pi/2$ - π - $\pi/2$ Bragg interferometer. The vertical (horizontal) direction represents space (time). See text for further details.

cloud and starts the slow cloud so that the two clouds come back together. The final pulse is applied after a time T_2 when the two clouds again overlap causing each cloud to split again. After a further time T_3 there is a pair of overlapping slow clouds and a pair of overlapping fast clouds that give rise to the final pattern that is imaged at that moment.

III. BRAGG INTERFEROMETER PROTOTYPER MODELS

The operation of an arbitrary Bragg AI can be specified by stating the times and angles of the Bragg pulses applied to the condensate. Although it is possible to apply a Bragg pulse having an arbitrary angle, θ , here we will restrict our attention to pulses where $\theta = \pi$ or $\theta = \pi/2$ radians. Hence these pulses will either split clouds into two equal pieces, one fast and one slow, or will leave the condensate whole and merely swap its fast or slow velocity. Thus we only consider interferometer sequences that are composed of $\pi/2$ and/or π pulses.

A. Overview of prototyper models

Our general prototyper model will enable us to approximate the evolution of the condensate wave function through all of the steps of any given interferometer sequence. We assume that the duration of all Bragg pulses is short compared to the characteristic time for collective effects of the condensate to be manifested. This time is usually \hbar/μ where μ is the chemical potential of the condensate. This means that we assume that any changes in the momentum space distribution of the condensate atoms caused by a Bragg pulse happen instantaneously. We further assume that the characteristic size of any mo-

mentum change is large in the sense that the wavelength of the photon causing the change is small compared to the size of the condensate. Finally we assume that the evolution of the condensate between pulses is governed by the Gross–Pitaevskii equation.

Our Bragg prototyper method therefore has two essential elements: (1) an approximation of the effect of a Bragg pulse on the condensate wave function, and (2) a model for approximating the GP–governed condensate wave function behavior between pulses. The method consists of applying these two elements to the pulse sequence of the given interferometer design to produce an approximate final condensate wave function so that predictions about the measured interference patterns can be made.

For the first element, as will be described in more detail below, we represent the condensate wave function at any moment as a superposition of a number of fast or slow gaussian clouds. We model the effect of Bragg pulses as follows. If the wave function for a given cloud in the condensate wave function is $\psi(\mathbf{r}, t)$ before the Bragg pulse, then the change in this wave function is, for

slow clouds:

$$\begin{aligned}\psi(\mathbf{r}, t) &\rightarrow \frac{1}{\sqrt{2}} (\psi(\mathbf{r}, t) - e^{-i\phi} e^{i\Delta\mathbf{k}\cdot\mathbf{r}} \psi(\mathbf{r}, t)) \quad (\pi/2 \text{ pulse}) \\ \psi(\mathbf{r}, t) &\rightarrow -e^{-i\phi} e^{i\Delta\mathbf{k}\cdot\mathbf{r}} \psi(\mathbf{r}, t) \quad (\pi \text{ pulse})\end{aligned}\quad (1)$$

and for **fast clouds:**

$$\begin{aligned}\psi(\mathbf{r}, t) &\rightarrow \frac{1}{\sqrt{2}} (e^{i\phi} \psi(\mathbf{r}, t) + e^{-i\Delta\mathbf{k}\cdot\mathbf{r}} \psi(\mathbf{r}, t)) \quad (\pi/2 \text{ pulse}) \\ \psi(\mathbf{r}, t) &\rightarrow e^{i\phi} e^{-i\Delta\mathbf{k}\cdot\mathbf{r}} \psi(\mathbf{r}, t) \quad (\pi \text{ pulse})\end{aligned}\quad (2)$$

where $\Delta\mathbf{k}$ is the momentum change for Bragg pulses defined above. The factor ϕ is the phase of the moving standing wave in the center of the initial atomic wavepacket in the middle of the Bragg pulse [32]. Thus the action of a $\pi/2$ pulse is to double the number of clouds, adding a new fast cloud on top of a previously existing slow cloud and adding a new slow cloud on top of a previously existing fast cloud. In each case the shape of the previously existing cloud is unchanged. The action of a π pulse is to convert a previously existing slow (fast) cloud into a fast (slow) cloud.

For the second element we use the Lagrangian Variational Method (LVM) [33, 34] to approximate the condensate evolution between pulses. Although it is possible to solve the 3D GP equation to determine this evolution, this is not practical for *rapid* estimation of the final condensate wave function. The LVM provides approximate solutions to the GP equation in the form of equations of motion for time–dependent parameters that appear in an assumed trial wave function. Thus the exact solution of the GP equation that requires the solution of a 3+1 partial differential equation is traded for approximate solutions that can be obtained by solving a system of ordinary differential equations in time. We briefly review this method now.

The GP equation is given by

$$i\hbar \frac{\partial \Psi}{\partial t} = -\frac{\hbar^2}{2m} \nabla^2 \Psi + V_{\text{trap}}(\mathbf{r}) \Psi + gN |\Psi|^2 \Psi \quad (3)$$

where we assume that any trapping potential is harmonic:

$$V_{\text{trap}}(\mathbf{r}) = \frac{1}{2} m \omega_x^2 x^2 + \frac{1}{2} m \omega_y^2 y^2 + \frac{1}{2} m \omega_z^2 z^2. \quad (4)$$

where m is the mass of a condensate atom.

Here we will introduce scaled variables that will be used throughout the rest of the paper. First we choose a length unit appropriate to the harmonic potential: $L_0 = (\hbar/2m\bar{\omega})^{1/2}$ where $\bar{\omega} = (\omega_x \omega_y \omega_z)^{1/3}$ and then define the energy unit as $E_0 = \hbar^2/2mL_0^2$ and the time unit as $T_0 = \hbar/E_0$. We then introduce scaled position and time variables as $\bar{x} = x/L_0, \bar{y} = y/L_0, \bar{z} = z/L_0, \bar{t} = t/T_0$, and use barred quantities in general to represent quantities expressed in the scaled units. If, additionally, we write the condensate wave function in scaled units as $\Psi = \bar{\Psi}/L_0^{3/2}$ then the GP equation becomes

$$i \frac{\partial \bar{\Psi}}{\partial \bar{t}} = -\bar{\nabla}^2 \bar{\Psi} + \bar{V}_{\text{trap}}(\bar{\mathbf{r}}) \bar{\Psi} + \bar{g}N |\bar{\Psi}|^2 \bar{\Psi} \quad (5)$$

where $\bar{\nabla}^2 = \partial^2/\partial \bar{x}^2 + \partial^2/\partial \bar{y}^2 + \partial^2/\partial \bar{z}^2$ and

$$\bar{V}_{\text{trap}}(\bar{\mathbf{r}}) = \frac{1}{4} \gamma_x^2 \bar{x}^2 + \frac{1}{4} \gamma_y^2 \bar{y}^2 + \frac{1}{4} \gamma_z^2 \bar{z}^2 \quad (6)$$

and where $\gamma_\eta = \omega_\eta/\bar{\omega}, \eta = x, y, z$ and $\bar{g} = g/(E_0 L_0^3)$.

The LVM produces equations of motion for the m time–dependent variational parameters that appear in a given trial wave function $\bar{\psi}_{\text{trial}}(\bar{\mathbf{r}}; q_1(t), \dots, q_m(t))$. The equations of motion are obtained from the LVM Lagrangian via the usual Euler–Lagrange equations of motion:

$$\frac{d}{d\bar{t}} \left(\frac{\partial L_{\text{LVM}}}{\partial \dot{q}_j} \right) - \frac{\partial L_{\text{LVM}}}{\partial q_j} = 0. \quad j = 1, \dots, m. \quad (7)$$

The LVM Lagrangian, in turn, is computed by integrating the LVM Lagrangian density

$$L_{\text{LVM}}(q_1(t), \dots, q_m(t)) = \int d^3r \mathcal{L} [\bar{\psi}_{\text{trial}}(\bar{\mathbf{r}}, t)]. \quad (8)$$

Finally, the LVM Lagrangian density that corresponds to the GP equation is given by

$$\begin{aligned}\mathcal{L}[\psi] &= \frac{i}{2} (\psi \psi_t^* - \psi^* \psi_t) + \bar{\nabla} \psi^* \cdot \bar{\nabla} \psi + \bar{V}_{\text{trap}}(\bar{\mathbf{r}}) |\psi|^2 \\ &\quad + \frac{1}{2} \bar{g} N |\psi|^4,\end{aligned}\quad (9)$$

where ψ_t denotes the partial derivative of ψ with respect to t . In order to get equations of motion relevant for a Bragg interferometer, we must choose a trial wave function. In this work we present equations of motion for single–cloud gaussian trial wave functions in three dimensions and two–cloud gaussian trial wave functions for both one and three dimensions.

An alternative approach to efficient approximate solution of the GP equation in interferometric applications has recently been presented by Jamison *et al.* [10]. It is based on a generalization of the Thomas–Fermi method originally proposed by Castin and Dum. [35]

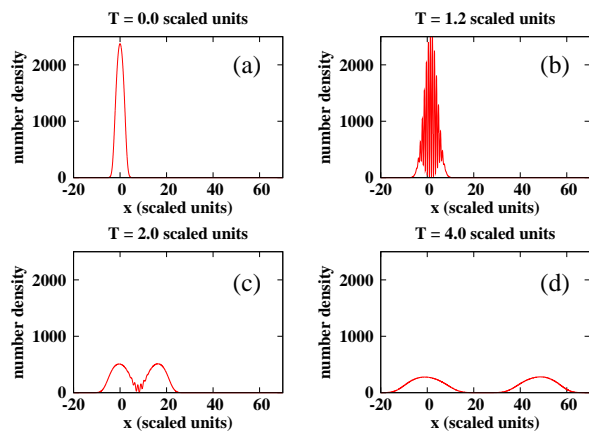


FIG. 2: (color online) This figure shows the evolution of a 1D condensate that is initially released and allowed to expand until $T = 1$ scaled time unit at which time a $\pi/2$ Bragg pulse is applied. The scaled velocity imparted by the Bragg pulse to the fast cloud is $\bar{v}_L = 16$ scaled velocity units. (a) The initial condensate density just after the trap is turned off, (b) after the $\pi/2$ Bragg pulse is applied, the density exhibits rapid oscillations in the region where the fast and slow clouds overlap, (c) and (d) nearly complete and complete separation. The value of $\bar{g}N = 10$ in scaled units.

B. 3D single-cloud LVM model

In the single-cloud LVM model we choose the trial wave function to have the form of a single, three-dimensional gaussian wavepacket, as was done previously in Ref. [33]

$$\bar{\Psi}(\bar{\mathbf{r}}, \bar{t}) = \bar{A}(t) \prod_{\eta=x,y,z} e^{-\frac{(\bar{\eta}-\bar{\eta}_0(\bar{t}))^2}{2\bar{w}_\eta^2(\bar{t})} + i\bar{\alpha}_\eta(\bar{t})\bar{\eta} + i\bar{\beta}_\eta(\bar{t})\bar{\eta}^2}. \quad (10)$$

Here $(\bar{x}_0, \bar{y}_0, \bar{z}_0)$ are the coordinates of the center of the wavepacket. The quantities $(\bar{\alpha}_x, \bar{\alpha}_y, \bar{\alpha}_z)$ are the linear phase coefficients which govern the motion of the wavepacket center. The $(\bar{w}_x, \bar{w}_y, \bar{w}_z)$ are the widths of the gaussian along the three axes and the $(\bar{\beta}_x, \bar{\beta}_y, \bar{\beta}_z)$ are the quadratic phase coefficients and govern the evolution of the widths. Finally, $\bar{A}(t)$ is a normalization coefficient that will be removed from the Lagrangian later when the normalization constraint is imposed. We can take \bar{A} to be real because, if \bar{A} had a phase, it would represent an overall wave function phase which would not be physical.

The equations of motion are derived as described above and the result is [33]

$$\begin{aligned} \ddot{\bar{\eta}}_0 + \gamma_\eta^2 \bar{\eta}_0 &= 0 \\ \ddot{\bar{w}}_\eta + \gamma_\eta^2 \bar{w}_\eta &= \frac{4}{\bar{w}_\eta^3} + \frac{2\bar{g}N}{(2\pi)^{3/2} \bar{w}_x \bar{w}_y \bar{w}_z \bar{w}_\eta} \\ \dot{\bar{\beta}}_\eta &= \frac{\dot{\bar{w}}_\eta}{4\bar{w}_\eta} \\ \dot{\bar{\alpha}}_\eta &= \frac{1}{2} \dot{\bar{\eta}}_0 - 2\bar{\beta}_\eta \dot{\bar{\eta}}_0 \quad \eta = x, y, z. \end{aligned} \quad (11)$$

It is worth noting that our equations of motion differ

slightly from those in Ref. [33] because of differences in the definition of scaled units.

C. NIST experiment and the single-cloud LVM model

A Bragg AI was implemented at NIST and used to image the phase evolution of an evolving Bose–Einstein condensate [30]. In that experiment, a condensate of about 1.8×10^6 sodium atoms was held in a magnetic trap with trapping frequencies $\omega_x = \sqrt{2}\omega_y = 2\omega_z = 2\pi \times 27$ Hz and subjected to $\pi/2-\pi-\pi/2$ pulse sequence. This sequence was performed both with the trap left on and with the trap turned off and the condensate allowed to expand for a time T_0 . With the trap on, the time conditions were fixed so that $T_1 = T_2 \equiv T$ where T was typically 1-2 ms and the clouds were allowed to expand in order for them to separate before imaging. In the trap-off case, a series of runs was carried out in which T_1 was held fixed at 1 ms while T_2 was varied such that the cloud overlap at the time of the final Bragg pulse ranged from fast cloud just arriving at the slow cloud until it had passed through and was just leaving. This series of runs was performed for an expansion time of $T_0 = 1$ ms and repeated for $T_0 = 4$ ms.

The results of this experiment were analyzed using the single-cloud LVM just described [30]. While the results of the single-cloud LVM model agreed well with experiment for runs performed with the trap on, it did not agree with experiment for trap-off cases. This discrepancy was due to the presence of an extra relative velocity between interfering clouds at the moment of the final Bragg pulse. The extra velocity was caused by repulsion between overlapping clouds which occurred just after the first $\pi/2$ pulse and again just before the second $\pi/2$ pulse. Agreement between theory and experiment was achieved by adding in by hand a small relative velocity correction to the condensate wave function predicted by the single-cloud model. It is clear that any model able to account for this repulsion would need to include at least two clouds. In order to derive a simple model we need to validate a key approximation by studying this correction for a single $\pi/2$ Bragg pulse.

IV. REPULSION STUDY FOR SINGLE $\pi/2$ BRAGG PULSE

Before turning to a two-cloud model, we studied the effects of fast/slow cloud repulsion on the final relative velocity of the separating clouds after a single $\pi/2$ Bragg pulse. We performed this study by simulating the application of such a pulse on a 1D condensate and its subsequent evolution by numerical solution of the GP equation.

In what follows we shall give the value of quantities in 1D scaled units which is a special case of the 3D scaled

units given above. In these units, all quantities are defined in terms of the length unit $L_0 = \sqrt{\hbar/2m\omega_0}$ which, in turn, is tied to a reference frequency, ω_0 . This frequency is often the trap frequency but need not be as in the case where the trap has been turned off. Since these quantities are scaled out of the problem, it will be useful to give a numerical example of the sizes of the scaled units. Thus, given a quasi-1D ^{87}Rb condensate confined in a $\omega = 2\pi \times 10$ Hz trap, the length unit is $L_0 = 2.4 \mu\text{m}$, the time unit is $T_0 = 15.8$ ms, and the velocity unit $v_0 = 0.015$ cm/s. The value of the interaction strength is varied over the range $0 \leq \bar{g}_{1D}N \leq 200$ so that the transition from non-interacting up to the Thomas-Fermi regime could be studied. Here, N is the number of condensate atoms.

Figure 2 shows a typical simulation where a condensate is released from the trap (panel (a)) and allowed to expand for until $T = 1$ scaled time unit at which time a $\pi/2$ Bragg pulse is applied splitting the condensate into fast (on the right) and slow clouds. During the separation the two clouds push each other apart so that the fast cloud moves with a velocity $\bar{v}_f = \bar{v}_L + \delta\bar{v}$ that is slightly larger than the recoil velocity \bar{v}_L caused by the laser light and the slow cloud drifts backwards with velocity $-\delta\bar{v}$. In SI units, the recoil velocity is $v_L = \hbar\Delta k/m$ and, in scaled units it can be expressed as $\bar{v}_L = v_L/(L_0/T_0) = 2\Delta\bar{k}$. The interaction strength of the initial condensate in this example was $\bar{g}N = 10$ in scaled units.

To study this velocity “kick”, $\delta\bar{v}$, we used the GP simulations to determine its value as a function of the interaction strength of the initial condensate. The value of $\delta\bar{v}$ for a given value of $\bar{g}N$ was obtained by running a simulation where a $\pi/2$ Bragg pulse was applied. The velocities of the fast and slow clouds were determined, for each value of $\bar{g}N$, as follows. In each run the two clouds were allowed to separate fully after the pulse; a midpoint between the two clouds, \bar{x}_{mid} , and a time after which both clouds were fully separated, \bar{t}_{sep} , were then determined; and then the expectation value of \bar{x} was computed numerically for each cloud separately at each time step in the range $\bar{t} \geq \bar{t}_{\text{sep}}$:

$$\begin{aligned} \bar{x}_{\text{slow}}(\bar{t}) &= \int_{-\bar{L}/2}^{\bar{x}_{\text{mid}}} \bar{x} |\bar{\Psi}(\bar{x}, \bar{t})|^2 d\bar{x} \\ &\equiv \bar{x}_{\text{slow}}(\bar{t}_{\text{sep}}) + \bar{v}_{\text{slow}}(\bar{t} - \bar{t}_{\text{sep}}) \\ \bar{x}_{\text{fast}}(\bar{t}) &= \int_{\bar{x}_{\text{mid}}}^{\bar{L}/2} \bar{x} |\bar{\Psi}(\bar{x}, \bar{t})|^2 d\bar{x} \\ &\equiv \bar{x}_{\text{fast}}(\bar{t}_{\text{sep}}) + \bar{v}_{\text{fast}}(\bar{t} - \bar{t}_{\text{sep}}) \end{aligned} \quad (12)$$

where \bar{L} is the length of the numerical grid used in the GP simulation. Care was taken to make sure that none of the clouds got close to the edges of the grid. Finally, the velocities of the fast and slow clouds were extracted by fitting straight lines to the \bar{x}_{slow} and \bar{x}_{fast} results to obtain \bar{v}_{slow} and \bar{v}_{fast} . The extra velocity “kicks” for each cloud due to repulsion were determined by $\delta\bar{v}_{\text{fast}} = \bar{v}_{\text{fast}} - \bar{v}_L$ and $\delta\bar{v}_{\text{slow}} = \bar{v}_{\text{slow}}$. Convergence runs of the

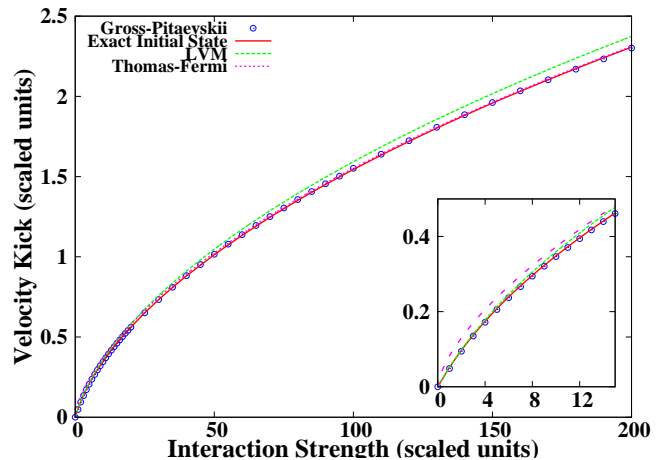


FIG. 3: (color online) This figure shows the velocity “kick”, $\delta\bar{v}$, versus interaction strength, $\bar{g}N$. The open circles are the results obtained from GP-equation simulations; the three curves show estimates of the velocity kick obtained by equating the difference in total kinetic energy of the interacting system and the non-interacting system with $2/3$ of the total interaction energy. These estimates are derived from (1) the exact GP initial state (solid curve), (2) LVM-approximate initial state (dashed curve) and (3) Thomas-Fermi approximate initial state (dotted curve).

GP solver for finer space and time steps showed that $\delta\bar{v}_{\text{slow}} = \delta\bar{v}_{\text{fast}} \equiv \delta\bar{v}$ over the entire interaction strength range. This shows that momentum was conserved and supports the picture of two equal-mass clouds pushing against each other as they separate.

Fig. 3 contains a graph of the velocity kick versus interaction strength for $0 \leq \bar{g}N \leq 200$. For this set of simulations, the Bragg pulse was applied and the trap was turned off simultaneously at $\bar{t} = 0$. For the results shown, the recoil velocity was $\bar{v}_L = 10$ scaled velocity units. In the example mentioned above this would give ^{87}Rb atoms a recoil velocity of 0.15 cm/s. The result displayed in Fig. 3 can be quantitatively understood in a simple way as we now explain.

The velocity kick, $\delta\bar{v}$, is the result of mutual repulsion between the fast and slow clouds as they separate after the Bragg pulse. From a classical viewpoint, this repulsion will result in a change in the total kinetic energy of the center-of-mass (CM) motion of the two clouds. Thus the difference between the total CM kinetic energy of the two interacting clouds and the kinetic energy of the two non-interacting clouds should be equal to the energy available for repulsion assuming the repulsion produces no distortion.

Since the Bragg pulse splits the N -atom condensate into two equal pieces we can express this equality as (we begin in SI units and then convert):

$$\begin{aligned} U_{\text{rep}} &= \left(\frac{N}{2}\right) \frac{1}{2}m(v_L + \delta v)^2 + \left(\frac{N}{2}\right) \frac{1}{2}m(\delta v)^2 \\ &\quad - \left(\frac{N}{2}\right) \frac{1}{2}mv_L^2 \end{aligned} \quad (13)$$

where U_{rep} is the many-body energy available for different clouds to repel each other. We can derive an expression for this from the total many-body interaction energy given by [20]

$$U_{\text{int}} = \frac{1}{2}N(N-1)g \int_{-\infty}^{\infty} dx |\Psi(x,t)|^4 \quad (14)$$

where $\Psi(x,t)$ is the condensate wave function after the $\pi/2$ Bragg pulse and has the general form

$$\Psi(x,t) = \psi_1(x,t) + e^{i\Delta k x} \psi_2(x,t). \quad (15)$$

We have chosen to distinguish between ψ_1 and ψ_2 , even though they are the same in our model, for bookkeeping purposes that will become apparent below. Substituting Eq. (15) into (14) we have

$$\begin{aligned} U_{\text{int}} = & \frac{g}{2}N(N-1) \int_{-\infty}^{\infty} dx \left[|\psi_1|^4 + |\psi_2|^4 + 4|\psi_1|^2|\psi_2|^2 \right. \\ & + \left. \left\{ 2(|\psi_1|^2 + |\psi_2|^2) \psi_1^* \psi_2 e^{i\Delta k x} + (\psi_1^* \psi_2)^2 e^{2i\Delta k x} \right. \right. \\ & \left. \left. + \text{c.c.} \right\} \right] \quad (16) \end{aligned}$$

Here we will make a crucial approximation. This approximation will be tested by comparison of the velocity kicks predicted here with those determined by numerical solution of the GP equation and will be used again in deriving a two-cloud LVM model.

We assume here that Δk is large enough so that all of the integrals containing exponentials such as $\exp(\pm i\Delta k x)$ and $\exp(\pm 2i\Delta k x)$ in Eq. (16) can be neglected. This is equivalent to assuming that the wavelength of the Bragg pulse light is small compared to the size of the condensate. Hence terms having these exponentials oscillate rapidly and the integrals containing them approximately average to zero. The result of this approximation is that all of the terms inside the curly braces in Eq. (16) can be neglected and we can write

$$\begin{aligned} U_{\text{int}} & \approx \frac{g}{2}N(N-1) \int_{-\infty}^{\infty} dx (|\psi_1|^4 + |\psi_2|^4 + 4|\psi_1|^2|\psi_2|^2) \\ & \equiv U_{\text{self},1} + U_{\text{self},2} + U_{\text{rep}}. \quad (17) \end{aligned}$$

This last expression suggests a picture of the evolution of fast and slow clouds during separation. This picture depends on two assumptions: (1) the separating clouds do not distort significantly so that the form of the wave function in Eq. (15) is maintained and, (2) the wavevector, Δk , is large enough so that the approximation in Eq. (17) is valid. In this case, the fast/slow cloud evolution during separation divides into three categories: (1) self interaction of the fast cloud, (2) self interaction of the slow cloud, and (3) fast/slow cloud interaction. The energy available for this last interaction is suggested by the

above equation:

$$\begin{aligned} U_{\text{rep}} & = \frac{1}{2}gN(N-1) \int_{-\infty}^{\infty} 4|\psi_1|^2|\psi_2|^2 dx \\ & \approx \frac{1}{2}gN^2 \int_{-\infty}^{\infty} |\psi|^4 dx = \frac{2}{3}U_{\text{int}}. \quad (18) \end{aligned}$$

Here we assume that $N \gg 1$ and that $\psi_1 \approx \psi_2 \approx \psi/\sqrt{2}$ where ψ is the (unit norm) condensate wave function *before* application of the Bragg pulse as in Eqs. (1) and (2).

This fact also leads to the last equality because, from Eq. (17), it is clear that the total energy of interaction is one part self interaction of cloud 1, one part self interaction of cloud 2, and 4 parts cloud-cloud interaction. The self interaction terms, according to our picture, are energies available for expansion while the cloud-cloud interaction either distorts the cloud shapes and/or changes the velocities of their centers-of-mass. We assume no distortion so all of this energy is assumed available for giving the clouds a velocity kick. We can now derive this kick by substituting the approximate expression for U_{rep} into Eq. (13) and canceling common factors of $N/2$:

$$\begin{aligned} gN \int_{-\infty}^{\infty} |\psi|^4 dx & = \frac{1}{2}m(v_L + \delta v)^2 + \frac{1}{2}m(\delta v)^2 \\ & - \frac{1}{2}mv_L^2 \\ \bar{g}N \int_{-\infty}^{\infty} |\bar{\psi}|^4 d\bar{x} & = \frac{1}{4}(\bar{v}_L + \delta \bar{v})^2 + \frac{1}{4}(\delta \bar{v})^2 \\ & - \frac{1}{4}\bar{v}_L^2, \quad (19) \end{aligned}$$

where in second line above we have converted back to scaled units. Thus we can now write an expression for the velocity kick:

$$\delta \bar{v} = \left[\frac{1}{4}\bar{v}_L^2 + 2\bar{u}_{sp} \right]^{1/2} - \frac{1}{2}\bar{v}_L, \quad (20)$$

where

$$\bar{u}_{sp} \equiv \bar{g}N \int_{-\infty}^{\infty} |\bar{\psi}|^4 d\bar{x} \quad (21)$$

and $\bar{v}_L = 2\Delta \bar{k}$. We can think of the separating clouds being pushed apart by a spring in between them and \bar{u}_{sp} is the initial energy stored in the spring.

The comparison of values of $\delta \bar{v}$ predicted by the above model with those determined from numerical solution of the GP equation are shown in Fig. 3. The discrete points are the numerically determined values and the remaining three curves are computed via Eq. (20) where \bar{u}_{sp} has been calculated using three expressions for ψ , the initial state condensate wave function. These three versions of ψ were (1) the exact initial state from the GP simulation (solid curve), (2) an LVM gaussian cloud where the gaussian width was the stationary value for a 1D condensate confined in the initial harmonic trap (dashed line), and (3) the Thomas-Fermi-approximate solution of the GP equation for the trapped condensate (dotted line).

All three expressions, as can be seen from the graph, gave good estimates. We found that using the exact GP initial state gave near-perfect agreement (to four decimal places) with the kick determined from numerical GP. The LVM gaussian performed very well for small $\bar{g}N$ and less well for large while the Thomas–Fermi works well for large $\bar{g}N$ and less well for small.

This agreement between the numerically determined kicks and the estimates from our heuristic model lends support to our picture of the effect of cloud/cloud interaction during separation. We will use this in what follows to develop a two-cloud LVM technique for modeling a full Bragg interferometer.

V. TWO-CLOUD LVM MODEL

In this section we present a two-cloud LVM model to approximate the evolution of the condensate wave function following a $\pi/2$ Bragg pulse. The presence of two clouds will enable the model to account for cloud–cloud interactions and should be able to predict the velocity kick accurately. Below we present both 1D and 3D versions of this model. This will enable us to make quantitative comparisons of our model with the results of 1D GP simulations of the entire $\pi/2$ – π – $\pi/2$ interferometer. The 3D model will be useful for assessment of real-world AI designs. In addition, we also present comparisons of our 3D two-cloud model with the results of the original NIST experiment.

A. 1D two-cloud LVM

The trial wave function for the 1D two-cloud LVM model is taken to be a sum of two 1D gaussian wavepackets where one of them is boosted to a velocity of $\bar{v}_L = 2\Delta\bar{k}$:

$$\bar{\Psi}(\bar{x}, \bar{t}) = \frac{\bar{A}_{1D}(\bar{t})}{\sqrt{2}} \left(e^{f_1(\bar{x}, \bar{t})} + e^{i\Delta\bar{k}\bar{x}} e^{f_2(\bar{x}, \bar{t})} \right) \quad (22)$$

where

$$f_j(\bar{x}, \bar{t}) \equiv -\frac{(\bar{x} - \bar{x}_j(\bar{t}))^2}{2\bar{w}^2(\bar{t})} + i\bar{\alpha}_j(\bar{t})\bar{x} + i\bar{\beta}(\bar{t})\bar{x}^2 \quad (23)$$

where $j = 1, 2$. We note here that both the slow cloud (cloud 1) and the fast cloud share the same width, \bar{w} , and quadratic phase curvature, $\bar{\beta}$ but have differing centers and linear phase coefficients. This assumption is borne out in multiple GP simulations as can be seen, for example, in Fig. 2. Imposing the normalization condition yields the following constraint: $|\bar{A}_{1D}|^2 \bar{w} \pi^{1/2} = 1$ where all terms containing exponentials such as $e^{\pm i\Delta\bar{k}\bar{x}}$ were neglected.

Carrying out the procedure described in Section III A, we calculate the LVM Lagrangian by inserting the trial

wave function into the Lagrangian density and integrating. If we neglect rapidly oscillating terms and impose the normalization constraint we obtain the following result.

$$\begin{aligned} \bar{L}_{1D} = & \frac{1}{2}\dot{\bar{\alpha}}_1\bar{x}_1 + \frac{1}{2}\dot{\bar{\alpha}}_2\bar{x}_2 + \frac{1}{2}\dot{\bar{\beta}}(\bar{x}_1^2 + \bar{x}_2^2 + \bar{w}^2) \\ & + \frac{1}{2\bar{w}^2} + \frac{1}{2}(\bar{\alpha}_1 + 2\bar{\beta}\bar{x}_1)^2 + \frac{1}{2}(\bar{\alpha}_2 + 2\bar{\beta}\bar{x}_2)^2 \\ & + (\Delta\bar{k})(\bar{\alpha}_2 + 2\bar{\beta}\bar{x}_2) + \frac{1}{2}(\Delta\bar{k})^2 + 2\bar{\beta}^2\bar{w}^2 \\ & + \frac{1}{8}\gamma^2(\bar{x}_1^2 + \bar{x}_2^2 + \bar{w}^2) \\ & + \left(\frac{\bar{g}N}{4(2\pi)^{1/2}\bar{w}} \right) \left(1 + 2e^{-(\bar{x}_1 - \bar{x}_2)^2/2\bar{w}^2} \right), \quad (24) \end{aligned}$$

where $\gamma = \omega/\omega_0$ is the ratio of the actual trap frequency to the frequency used to define the length unit.

We find the equations of motion using the ordinary Euler–Lagrange equations (see Eq. (7)). After some rearrangement these equations can be expressed as follows:

$$\begin{aligned} \ddot{\bar{x}}_1 + \gamma^2\bar{x}_1 &= F_{12}^{(1D)}(\bar{x}_1, \bar{x}_2, \bar{w}) \\ \ddot{\bar{x}}_2 + \gamma^2\bar{x}_2 &= -F_{12}^{(1D)}(\bar{x}_1, \bar{x}_2, \bar{w}) \\ \ddot{\bar{w}} + \gamma^2\bar{w} &= F_w^{(1D)}(\bar{x}_1, \bar{x}_2, \bar{w}) \quad (25) \end{aligned}$$

where

$$F_{12}^{(1D)}(\bar{x}_1, \bar{x}_2, \bar{w}) \equiv \left(\frac{2\bar{g}N}{(2\pi)^{1/2}\bar{w}^3} \right) (\bar{x}_1 - \bar{x}_2) e^{-(\bar{x}_1 - \bar{x}_2)^2/2\bar{w}^2} \quad (26)$$

and

$$\begin{aligned} F_w^{(1D)}(\bar{x}_1, \bar{x}_2, \bar{w}) &\equiv \frac{4}{\bar{w}^3} + \left(\frac{\bar{g}N}{(2\pi)^{1/2}\bar{w}^2} \right) \\ &\times \left[1 + 2 \left(1 - \frac{(\bar{x}_1 - \bar{x}_2)^2}{\bar{w}^2} \right) e^{-(\bar{x}_1 - \bar{x}_2)^2/2\bar{w}^2} \right] \quad (27) \end{aligned}$$

where $F_{12}^{(1D)}$ can be thought of as the “force” of repulsion between the separating clouds and $F_w^{(1D)}$ roughly thought of as the “force” causing the width to change.

The above equations constitute a closed system of equations to be solved for \bar{x}_1 , $\dot{\bar{x}}_1$, \bar{x}_2 , $\dot{\bar{x}}_2$, \bar{w} , and $\dot{\bar{w}}$. Once these equations are solved, the remaining parameters appearing in the trial wave function can be obtained as follows.

$$\begin{aligned} \bar{\beta} &= \frac{\dot{\bar{w}}}{4\bar{w}} \\ \bar{\alpha}_1 &= \frac{1}{2}\dot{\bar{x}}_1 - 2\bar{\beta}\bar{x}_1 \\ \bar{\alpha}_2 &= \frac{1}{2}\dot{\bar{x}}_2 - 2\bar{\beta}\bar{x}_2 - \Delta\bar{k} \quad (28) \end{aligned}$$

The above system of equations have some interesting properties that are analogous to those for Newton’s second law. For example, if we introduce the center of mass of the two-cloud system, $\bar{x}_{cm} \equiv (\bar{x}_1 + \bar{x}_2)/2$, and the relative coordinate, $\bar{x}_{rel} \equiv \bar{x}_1 - \bar{x}_2$ we find their equations of motion by adding and subtracting the first two of Eqs. (25) respectively. They are

$$\begin{aligned} \ddot{\bar{x}}_{cm} + \gamma^2\bar{x}_{cm} &= 0 \\ \ddot{\bar{x}}_{rel} + \gamma^2\bar{x}_{rel} &= 2F_{12}^{(1D)}(\bar{x}_1, \bar{x}_2, \bar{w}) \equiv 2F_{12}^{(1D)}(\bar{x}_{rel}, \bar{w}) \quad (29) \end{aligned}$$

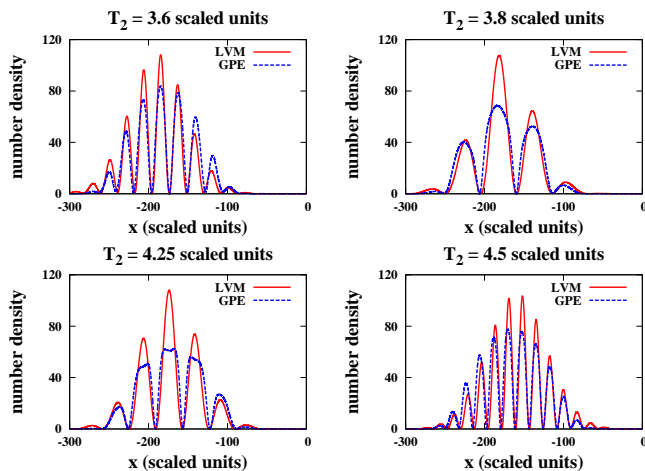


FIG. 4: (color online) These plots show a comparison of the interference patterns resulting from a $\pi/2-\pi-\pi/2$ Bragg AI computed by the GP equation (dashed line) and by the Bragg prototyper method. The interferometer times were (in scaled time units) $T_0 = 1$, $T_1 = 4$, T_2 variable, and $T_3 = 13.4$. The times for T_2 are (clockwise from upper left) $T_2 = 3.6, 3.8, 4.25, 4.5$ scaled time units. The interaction strength for all runs was $\bar{g}N = 10$ scaled units.

where, in the last equality, we noted that $F_{12}^{(1D)}$ only depends on the relative coordinate and the width. The first of the above equations can be solved immediately by inspection and is equivalent to the classical result that the CM motion of a system only depends on external forces. This reduces the total number of equations that must be solved numerically to the equation for \bar{w} in Eqs. (25) and the equation for \bar{x}_{rel} above.

There is also a conserved “energy” that can be written as

$$\bar{E}_{1D} = \frac{1}{2}\dot{\bar{x}}_1^2 + \frac{1}{2}\dot{\bar{x}}_2^2 + \frac{1}{2}\dot{\bar{w}}^2 + \bar{U}_{1D}(\bar{x}_1, \bar{x}_2, \bar{w}) \quad (30)$$

where the “potential energy” \bar{U}_{1D} is given by

$$\begin{aligned} \bar{U}_{1D}(\bar{x}_1, \bar{x}_2, \bar{w}) &= \frac{1}{2}\gamma^2\bar{x}_1^2 + \frac{1}{2}\gamma^2\bar{x}_2^2 + \frac{1}{2}\gamma^2\bar{w}^2 + \frac{2}{\bar{w}^2} \\ &+ \left(\frac{\bar{g}N}{(2\pi)^{1/2}\bar{w}}\right) \left(1 + 2e^{-(\bar{x}_1 - \bar{x}_2)^2/2\bar{w}^2}\right). \end{aligned} \quad (31)$$

Equations (25) can all be written as the second time derivative of each coordinate equals the negative partial derivative of the above potential energy with respect to the corresponding coordinate (e.g., $\ddot{\bar{x}}_1 = -\partial\bar{U}_{1D}/\partial\bar{x}_1$). This constant of the motion can be used to estimate the velocity kick and is also useful as a check on numerics.

Equations (25) and (28) can be used with the rest of the Bragg prototyper model to simulate Bragg AI behavior. We have used this 1D Bragg prototyper model to predict the results of a $\pi/2-\pi-\pi/2$ Bragg AI and have also simulated such an AI with the 1D GP equation. In these runs, the condensate was released from the trap and

allowed to expand for $T_0 = 1$ scaled time unit. The $\pi/2$ Bragg pulse was then applied and, after a time interval $T_2 = 4$ scaled units, a π pulse was applied followed by a variable time interval, T_2 , at which time the final Bragg pulse was turned on. The clouds were allowed to evolve for an additional $T_3 = 13.4$ time units. Figure 4 shows the comparison of the interference patterns predicted by the Bragg prototyper model and by the GP equation. Each graph corresponds to a different value of T_2 . In the figure, the values were (clockwise from upper left panel) $T_2 = 3.6, 3.8, 4.25, 4.5$ time units.

The GP equation was solved using a Crank–Nicolson algorithm on a space grid of width $\bar{L} = 800$ length units and divided into $N_x = 32768$ space steps over a total time of $\bar{t}_{max} = 22$ scaled time units using $N_t = 1200000$ time steps. The initial state was computed by integrating the GP equation in imaginary time with the trap on. The time needed to obtain fully converged final interference patterns was about five hours of run time on a commodity laptop. The time required to obtain the model results on the same computer was about 1 second, approximately 18,000 times faster. We expect that the speedup factor for 3D solutions to be 2–3 orders-of-magnitude greater. This makes our model an essential tool for assessment of more complicated atom interferometers which result from new AI designs inspired by quantum information science.

It is easy to see that the Bragg prototyper model reproduces the number and spacing of the GP–equation interference fringes in all cases. The major difference is that the width and height of the GP fringes are wider and shorter, respectively, than those in the LVM pattern. It is likely that the area under the curve in corresponding GP and LVM fringes is the same. This would make wider fringes lower and would imply that the number of atoms in each GP fringe was approximately equal to the number of atoms in the corresponding LVM fringe.

B. 3D two–cloud LVM

We also derived a 3D version of the two–cloud LVM model. The derivation is a straightforward generalization of the 1D version with all of the same assumptions and approximations. We include the highlights of its derivation for completeness.

The trial wavefunction for the 3D two–cloud LVM model is a sum of two 3D gaussians:

$$\Psi(\bar{\mathbf{r}}, \bar{t}) = \frac{\bar{A}_{3D}}{\sqrt{2}} \left(e^{F_1(\bar{\mathbf{r}}, \bar{t})} + e^{i\Delta\bar{\mathbf{k}}\cdot\bar{\mathbf{r}}} e^{F_2(\bar{\mathbf{r}}, \bar{t})} \right) \quad (32)$$

where

$$F_j(\bar{\mathbf{r}}, \bar{t}) = \sum_{\eta=x,y,z} \left(-\frac{(\bar{\eta} - \bar{\eta}_j)^2}{2\bar{w}_\eta^2} + i(\bar{\alpha}_{j\eta}\bar{\eta} + \bar{\beta}_\eta\bar{\eta}^2) \right) \quad (33)$$

and $j = 1, 2$. In three dimensions we allow for the possibility of differing widths, \bar{w}_η , $\eta = x, y, z$ along the

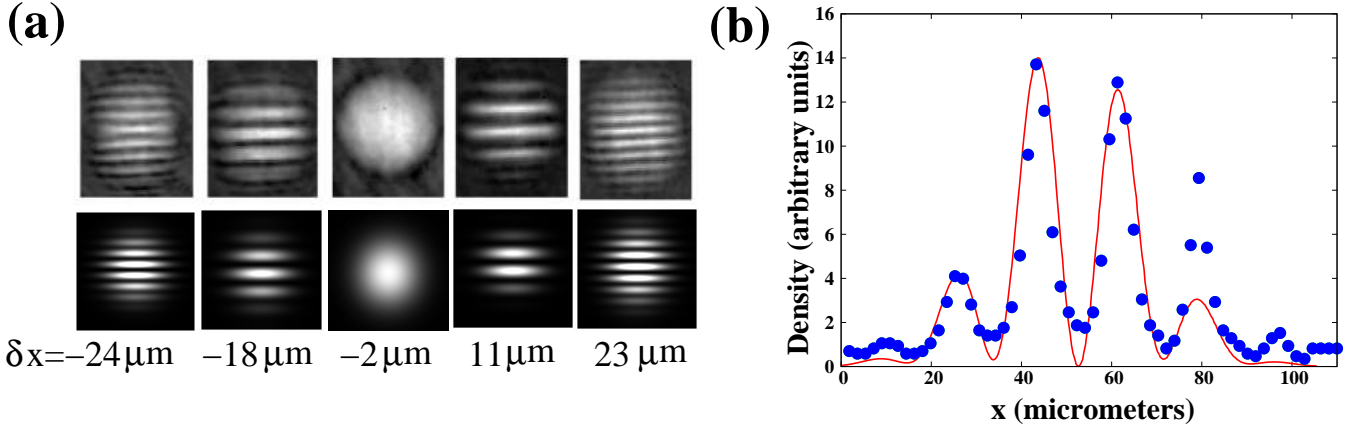


FIG. 5: (color online) This figure exhibits a comparison of the results of the 3D two-cloud Bragg AI model with the experimental results given in Fig. 2 of Ref. [30] where the NIST experiment discussed earlier in the text was described. In that experiment, the evolving phase of a Bose-Einstein condensate wave function was probed using a $\pi/2-\pi-\pi/2$ Bragg interferometer. (a) Interference patterns obtained for interferometer runs (top row experiment, bottom row theory) where $T_0 = 4$ ms, $T_1 = 1$ ms, $T_3 = 2$ ms, and T_2 was varied so that the cloud-center spacings (δx) at the last Bragg pulse were the values given in the figure; (b) A quantitative comparison of the case for $\delta x = 11\mu\text{m}$ (second from right end in panel (a)). The theory curve was normalized to match the highest experimental peak.

three axes, however we assume that these widths are the same for both clouds. This holds for the corresponding phase curvature coefficients $\bar{\beta}_\eta$, $\eta = x, y, z$ as well. It is straightforward to calculate the normalization constraint as $|\bar{A}_{3D}|^2 \bar{w}_x \bar{w}_y \bar{w}_z \pi^{1/2} = 1$. We note again that it was necessary to neglect rapidly oscillating terms that contained exponentials such as $e^{\pm i \Delta \bar{k} \cdot \bar{\mathbf{r}}}$ to arrive at this result.

The Lagrangian for this trial wave function thus becomes

$$\begin{aligned} \bar{L}_{3D} = & \sum_{\eta=x,y,z} \left\{ \frac{1}{2} \dot{\bar{\alpha}}_{1\eta} \bar{\eta}_1 + \frac{1}{2} \dot{\bar{\alpha}}_{2\eta} \bar{\eta}_2 + \frac{1}{2} \dot{\bar{\beta}}_\eta (\bar{\eta}_1^2 + \bar{\eta}_2^2 + \bar{w}_\eta^2) \right. \\ & + \frac{1}{2} (\bar{\alpha}_{1\eta} + 2\bar{\beta}_\eta \bar{\eta}_1)^2 + \frac{1}{2} (\bar{\alpha}_{2\eta} + 2\bar{\beta}_\eta \bar{\eta}_2 + \Delta \bar{k}_\eta)^2 \\ & \left. + \frac{1}{2\bar{w}_\eta^2} + 2\bar{\beta}_\eta^2 \bar{w}_\eta^2 + \frac{1}{8} \gamma_\eta^2 (\bar{\eta}_1^2 + \bar{\eta}_2^2 + \bar{w}_\eta^2) \right\} \\ & + \left(\frac{\bar{q}N}{4(2\pi)^{3/2} \bar{w}_x \bar{w}_y \bar{w}_z} \right) \left(1 + 2e^{-\sum_{\eta=x,y,z} \frac{(\bar{\eta}_1 - \bar{\eta}_2)^2}{2\bar{w}_\eta^2}} \right) \end{aligned} \quad (34)$$

where $\gamma_\eta \equiv \omega_\eta / \bar{\omega}$ and $\bar{\omega}$ is the geometric average of the three trap frequencies that is used in the definition of the 3D length unit.

The equations of motion that arise from the above Lagrangian are

$$\begin{aligned} \ddot{\bar{\eta}}_1 + \gamma_\eta^2 \bar{\eta}_1 &= F_{12\eta}^{(3D)}(\bar{\mathbf{r}}_1, \bar{\mathbf{r}}_2, \bar{\mathbf{w}}) \\ \ddot{\bar{\eta}}_2 + \gamma_\eta^2 \bar{\eta}_2 &= -F_{12\eta}^{(3D)}(\bar{\mathbf{r}}_1, \bar{\mathbf{r}}_2, \bar{\mathbf{w}}) \\ \ddot{\bar{w}}_\eta + \gamma_\eta^2 \bar{w}_\eta &= F_{w\eta}^{(3D)}(\bar{\mathbf{r}}_1, \bar{\mathbf{r}}_2, \bar{\mathbf{w}}) \quad \eta = x, y, z. \end{aligned} \quad (35)$$

where $\bar{\mathbf{r}}_j \equiv (\bar{x}_j, \bar{y}_j, \bar{z}_j)$ with $j = 1, 2$ and $\bar{\mathbf{w}} \equiv (\bar{w}_x, \bar{w}_y, \bar{w}_z)$ and where the “force” terms on the right-hand-sides

above are given by

$$\begin{aligned} F_{12\eta}^{(3D)}(\bar{\mathbf{r}}_1, \bar{\mathbf{r}}_2, \bar{\mathbf{w}}) &= \left(\frac{2\bar{q}N}{(2\pi)^{3/2} \bar{w}_x \bar{w}_y \bar{w}_z \bar{w}_\eta} \right) \left(\frac{\bar{\eta}_1 - \bar{\eta}_2}{\bar{w}_\eta} \right) \\ &\times e^{-\sum_{\eta=x,y,z} \frac{(\bar{\eta}_1 - \bar{\eta}_2)^2}{2\bar{w}_\eta^2}} \\ F_{w\eta}^{(3D)}(\bar{\mathbf{r}}_1, \bar{\mathbf{r}}_2, \bar{\mathbf{w}}) &= \frac{4}{\bar{w}_\eta^3} + \left(\frac{\bar{q}N}{(2\pi)^{3/2} \bar{w}_x \bar{w}_y \bar{w}_z \bar{w}_\eta} \right) \left[1 + \right. \\ &\left. 2 \times \left(1 - \frac{(\bar{\eta}_1 - \bar{\eta}_2)^2}{\bar{w}_\eta^2} \right) e^{-\sum_{\eta=x,y,z} \frac{(\bar{\eta}_1 - \bar{\eta}_2)^2}{2\bar{w}_\eta^2}} \right] \end{aligned} \quad (36)$$

The rest of the equations connect the widths, and CM positions and velocities to the parameters that actually appear in the trial wave function. These are

$$\begin{aligned} \bar{\beta}_\eta &= \frac{\dot{\bar{w}}_\eta}{4\bar{w}_\eta} \\ \bar{\alpha}_{1\eta} &= \frac{1}{2} \dot{\bar{\eta}}_1 - 2\bar{\beta}_\eta \bar{\eta}_1 \\ \bar{\alpha}_{2\eta} &= \frac{1}{2} \dot{\bar{\eta}}_2 - 2\bar{\beta}_\eta \bar{\eta}_2 - \Delta \bar{k}_\eta \\ \eta &= x, y, z. \end{aligned} \quad (37)$$

The 3D version of the 2-cloud model shares some of the properties associated with the 1D version. These include (1) the motion of the CM, $\bar{\mathbf{r}}_{cm} = (\bar{\mathbf{r}}_1 + \bar{\mathbf{r}}_2)/2$ is governed only by the trapping force and, (2) there is a conserved energy given by

$$\bar{E}_{3D} = \frac{1}{2} \sum_{\eta=x,y,z} \{ \dot{\bar{\eta}}_1^2 + \dot{\bar{\eta}}_2^2 + \dot{\bar{w}}_\eta^2 \} + \bar{U}_{3D}(\bar{\mathbf{r}}_1, \bar{\mathbf{r}}_2, \bar{\mathbf{w}}) \quad (38)$$

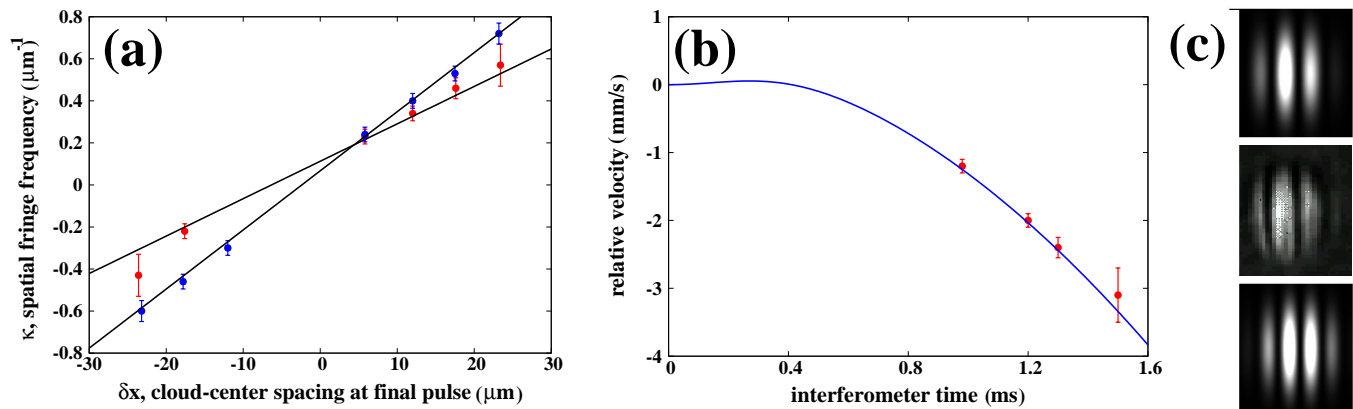


FIG. 6: (color online) (a) The spatial fringe frequency versus the cloud separation at the instant the final $\pi/2$ pulse is applied. The data is taken from Fig. 3 of Ref. [30]. The steeper line corresponds to $T_0 = 4$ ms, and the other line to $T_0 = 1$ ms. (b) The relative velocity between interfering clouds versus T , the interferometer time. Data is taken from Fig. 5 of the cited paper. (c) An interference pattern comparison between 3D one-cloud LVM (bottom), experiment (middle), and 3D two-cloud LVM (top), with the trap on during all the steps of the interferometer and $T = 1$ ms.

where

$$\begin{aligned} \bar{U}_{3D}(\bar{\mathbf{r}}_1, \bar{\mathbf{r}}_2, \bar{\mathbf{w}}) &= \sum_{\eta=x,y,z} \left\{ \frac{1}{2} \gamma_{\eta}^2 (\bar{\eta}_1^2 + \bar{\eta}_2^2 + \bar{w}_{\eta}^2) + \frac{2}{\bar{w}_{\eta}^2} \right\} \\ &+ \left(\frac{\bar{q}N}{(2\pi)^{3/2} \bar{w}_x \bar{w}_y \bar{w}_z} \right) \\ &\times \left(1 + 2 e^{-\sum_{\eta=x,y,z} \frac{(\bar{\eta}_1 - \bar{\eta}_2)^2}{2\bar{w}_{\eta}^2}} \right). \end{aligned} \quad (39)$$

These equations can now be used as a part of the two-gaussian-cloud LVM method to predict the behavior of atom interferometers. We have applied this model to the NIST experiment described earlier and detailed in Ref. [30]. Figure 5(a) shows interference patterns obtained in the experiment (top row) compared with the model. The timings of interferometer runs that produced these patterns were $T_0 = 4$ ms, $T_1 = 1$ ms, and $T_3 = 2$ ms. The values of T_2 were varied so that the spacing of the cloud centers, at the moment the final Bragg pulse is applied, δx , was as shown in Fig. 5(a).

We see that there is good agreement with the experimental patterns in terms of number and spacing of fringes. Figure 5(b) shows a more quantitative comparison for the case of $\delta x = 11 \mu\text{m}$. The data was taken from Fig. 2 of Ref. [30] and the theory is the result of the 3D two-cloud Bragg AI prototyper. All of these experiments were carried out with the trapping potential turned off. Since the kick is included naturally in our model, there was no need to add a velocity kick correction to achieve this level of agreement as there was for the one-cloud model.

In the NIST experiment, the spatial fringe frequency, κ , at the last Bragg pulse was measured as a function of δx for the trap off case. The comparison of these results with the 3D two-cloud LVM is shown in Fig. 6(a)

where the data is taken from Fig. 3 of Ref. [30]. In our LVM method, the atom density at the time of the last pulse oscillates as $\cos((\alpha_{2x} - \alpha_{1x})x)$. Thus we have $\kappa_{LVM} = \alpha_{2x} - \alpha_{1x}$ evaluated at the time of the last pulse. The above comparison shows excellent agreement with experiment. The relative velocity between the clouds in a given pair was also measured for different values of $T_1 = T_2 \equiv T$ when the trap was left on. The data from Fig. 5(b) of Ref. [30] is shown in Fig. 6(b) along with the results of the LVM for the relative velocity versus T . Again we find good agreement with the experiment.

The Fig. 6(c) shows a comparison of the 3D one-cloud LVM (bottom), 3D two-cloud LVM (top), and experiment (middle), for the interference pattern resulting from an interferometer run in which the trap was on and $T = 1$ ms. Although the one-cloud and two-cloud LVM interference patterns are both qualitatively similar to the experimental one, it is clear that the two-cloud pattern agrees better. Thus the apparent agreement between the one-cloud LVM and experiment presented in Ref. [30] in the trap-on case without the correction was fortuitous.

VI. DISCUSSION

In this paper we have presented a method suitable for rapid estimation of interference patterns deriving from ultra-cold Bragg atom interferometers. The method achieves this by representing the condensate wave function as a superposition of fast and slow gaussian clouds and then modeling the changes caused by (1) Bragg $\pi/2$ and π pulses and (2) by approximating the GP-equation evolution of the wave function during the intervals between the pulses. Thus, by following the sequence of Bragg pulses and intervals that occur in a particular Bragg AI, it is possible to approximate rapidly the final

condensate wave function and thus calculate the expected interference pattern.

In this model, Bragg pulses are assumed to change the wave function by instantaneous shifts in momentum space while *rapid* estimation of the effect of GP evolution is approximated using an LVM technique. We have validated the 1D version of this method by comparing its results with 1D numerical simulations of Mach–Zehnder–type atom interferometers using the GP equation. The 3D version was validated by comparison with experimental results presented in Ref. [30]. We found that the method provides good agreement with interference patterns in both the 1D and 3D cases as regards the number and spacing of fringes. In the 1D case, we found that our model obtained the final interference patterns at least 10,000 times faster than direct GP–equation simulation on the same computer. We expect this factor to be several orders–of–magnitude greater for the 3D case.

While the comparison of the results of the method with 1D GP simulations and with 3D experiment is quite good, there are some differences. In the 1D case, we found that it was necessary to shift our interference patterns over to line up fringe locations with the GP results. The shifts were small; they were at most 10 scaled length units which was a small difference compared to the width of a fringe. We did not have enough information about the experiment to determine if this was necessary in the 3D case. Also, as can be seen in Fig. 4(a), the fringe heights differ from the GP pattern. This difference is also present in the 3D comparison.

There are several possible reasons for these differences. First, our model tacitly assumes that separating clouds are not distorted by their mutual interaction since we model them as gaussians. In the 1D case, this assumption holds reasonably but not perfectly well over the range of $\bar{g}N$ considered. GP simulations with larger and larger $\bar{g}N$ values show that clouds become more and more distorted as the interaction strength increases. Thus some of the energy available for repulsion can be diverted from changing the CM velocity into cloud distortion.

Another reason for the difference may lie in our treatment of interacting clouds between the final Bragg pulse (which creates two fast and two slow clouds) and the time that an image is taken. During this interval, we use the two–cloud model to propagate each fast/slow pair separately and combine them at the end. This neglected the interaction of the overlapping clouds (the two fast clouds overlap and the two slow clouds overlap) as the two cloud pairs move apart. In fact, the T_3 interval is usually longer than all of the other intervals combined so there is ample opportunity for the two clouds in a pair to repel each other. This could be accounted for in a four–cloud model.

We also presented a study of the extra velocity kick that the slow and fast clouds receive when a $\pi/2$ Bragg pulse is applied to a condensate. When the condensate splits, the two clouds push against each other as they separate. This causes the fast cloud to acquire an extra

velocity, $\delta\bar{v}$, in addition to the velocity, \bar{v}_L , imparted by the light. The slow cloud recoils at velocity $\delta\bar{v}$ due to conservation of momentum. This study was conducted in 1D where the evolution of the condensate was simulated with the GP equation and the value of $\delta\bar{v}$ was determined directly from the simulation as a function of the interaction strength $\bar{g}N$. The values of $\bar{g}N$ ranged from non–interacting up to well into the Thomas–Fermi regime.

We found that these velocity kicks could be precisely predicted by setting the energy available for repulsion equal to the total kinetic energy of the interacting system minus the kinetic energy of the non–interacting system. We approximated the energy available for repulsion from the expression for the total interaction energy by neglecting rapidly oscillating terms involving the wavevector of the Bragg pulse light. The success of this procedure in reproducing the velocity kicks reinforces the picture of the interaction energy being partitioned into self–interaction energy of individual clouds and energy for cloud–cloud interaction. And furthermore, that the cloud–cloud interaction only produces a CM velocity change.

It is also important to mention that there are some phenomena that occur in Bragg atom interferometers that the model described in this paper might be modified to handle. Bragg processes often result in elastic scattering into initially unoccupied transverse momentum modes [36]. While these processes are not treated by the GP equation, it is possible to modify the effect of a pulse in these cases by adding clouds that occupy these momentum modes and neglecting their interaction with the mother condensate during separation. These modifications may also address other wave mixing processes that sometimes occur. Stray light can also cause problems for Bragg atom interferometers especially for condensates trapped near an atom chip. The major effect of stray light in these cases is to change the internal energy state of the atom. The model described above can be generalized to account for multiple internal levels of the atoms.

Another difficulty for Bragg interferometers is imperfections in the Bragg pulse wavefront which causes the laser intensity to vary across the condensate. In this case, different condensate atoms experience different pulse areas which causes the “angle” of the Bragg pulse to vary. That is, not all atoms will experience either a π or $\pi/2$ pulse. Our model can also be generalized to handle Bragg pulses of arbitrary angle. These “angle” errors in the pulses are analogous to imperfections in the thickness of the blades in a neutron interferometer. Such errors can be addressed by a new AI design that implements this QIS idea of the “power of one qubit” [37]. The implementation of this idea for Bragg interferometers will be the subject of a forthcoming article.

Atom interferometry with Bose–Einstein condensates hold the promise for applications in ultra–sensitive navigation and precision metrology. We noted earlier the idea that, because of the connection between quantum algo-

rithms and multi-particle interferometers, there is great potential for using the advances in QIS to inspire advances in precision interferometer designs. The Bragg AI prototyping method presented here represents a new tool for the rapid assessment of new Bragg AI designs. In the future we intend to apply our tool to design AIs that use QIS ideas for decoherence avoidance (e.g., decoherence-free subspaces, [38]) and minimization (e.g., the power of one qubit, [37]).

Acknowledgments

The authors acknowledge stimulating discussions with E. Hagley. This work was supported by the NSF under grant numbers PHY-1004975, PHY-0758111, the Physics Frontier Center grant PHY-0822671 and by NIST. The authors also acknowledge assistance from Hedayat Seddiqi.

-
- [1] D. A. Pushin, M. Arif, and D. G. Cory, *Phys. Rev. A* **79**, 053635 (2009).
- [2] D. A. Pushin, M. G. Huber, M. Arif, and D. G. Cory, *Phys. Rev. Lett.* **107**, 150401 (2011).
- [3] L. Hackermüller, S. Uttenthaler, K. Hornberger, E. Reiger, B. Brezger, A. Zeilinger, and M. Arndt, *Phys. Rev. Lett.* **91**, 090408 (2003).
- [4] S. Gerlich, M. Gring, H. Ulbricht, K. Hornberger, J. Tüxen, M. Mayor, and M. Arndt, *Angew. Chem. Int. Ed.* **47**, 6195 (2008).
- [5] M.-O. Mewes, M. R. Andrews, D. M. Kurn, D. S. Durfee, C. G. Townsend, and W. Ketterle, *Phys. Rev. Lett.* **78**, 582 (1997).
- [6] I. Bloch, T. W. Hänsch, and T. Esslinger, *Phys. Rev. Lett.* **82**, 3008 (1999).
- [7] L. Deng, E. W. Hagley, J. Denschlag, J. E. Simsarian, M. Edwards, C. W. Clark, K. Helmerson, S. L. Rolston, and W. D. Phillips, *Phys. Rev. Lett.* **83**, 5407 (1999).
- [8] M. Kozuma, Y. Suzuki, Y. Torii, T. Sugiura, T. Kuga, E. W. Hagley, and L. Deng, *Science* **286**, 2309 (1999).
- [9] R. Bouchendira, P. Cladé, S. Guellati-Khélifa, F. Nez, and F. Biraben, *Phys. Rev. Lett.* **106**, 080801 (2011).
- [10] A. O. Jamison, J. N. Kutz, and S. Gupta, *ArXiv e-prints* (2011), 1103.1454.
- [11] S. M. Tan and D. F. Walls, *Phys. Rev. A* **47**, 4663 (1993).
- [12] A. Peters, K. Chung, and S. Chu, *Metrologia* **38**, 25 (2001).
- [13] J. M. McGuirk, G. T. Foster, J. B. Fixler, M. J. Snadden, and M. A. Kasevich, *Phys. Rev. A* **65**, 033608 (2002).
- [14] T. Gustavson, P. Bouyer, and M. Kasevich, *Classical Quantum Gravity* **17**, 2385 (2000).
- [15] A. Miffre, M. Jacquy, M. Buchner, G. Trenec, and J. Vigué, *European Journal of Physics D* **38**, 353 (2006).
- [16] A. D. Cronin, J. Schmiedmayer, and D. E. Pritchard, *Rev. Mod. Phys.* **81**, 1051 (2009).
- [17] M. Anderson, J. Ensher, M. Matthews, C. Wieman, and E. Cornell, *Science* **269**, 198 (1995).
- [18] C. C. Bradley, C. A. Sackett, J. J. Tollett, and R. G. Hulet, *Phys. Rev. Lett.* **75**, 1687 (1995).
- [19] K. B. Davis, M. O. Mewes, M. R. Andrews, N. J. van Druten, D. S. Durfee, D. M. Kurn, and W. Ketterle, *Phys. Rev. Lett.* **75**, 3969 (1995).
- [20] C. Pethick and H. Smith, *Bose-Einstein Condensation in Dilute Gases* (Cambridge University Press, 2008), 2nd ed.
- [21] L. Pitaevskii and S. Stringari, *Bose-Einstein Condensation* (Oxford University Press, 2003).
- [22] S. Gupta, K. Dieckmann, Z. Hadzibabic, and D. E. Pritchard, *Phys. Rev. Lett.* **89**, 140401 (2002).
- [23] D. Döring, G. McDonald, J. E. Debs, C. Figl, P. A. Altin, H.-A. Bachor, N. P. Robins, and J. D. Close, *Phys. Rev. A* **81**, 043633 (2010).
- [24] M. Vengalattore, J. M. Higbie, S. R. Leslie, J. Guzman, L. E. Sadler, and D. M. Stamper-Kurn, *Phys. Rev. Lett.* **98**, 200801 (2007).
- [25] J. H. T. Burke, B. Deissler, K. J. Hughes, and C. A. Sackett, *Phys. Rev. A* **78**, 023619 (2008).
- [26] M. Olshanii and V. Dunjko (2005), *arXiv:cond-mat/0505358*.
- [27] J. A. Stickney, R. P. Kafle, D. Z. Anderson, and A. A. Zozulya, *Phys. Rev. A* **77**, 043604 (2008).
- [28] J. Debs, P. Altin, T. Barter, D. Döring, G. Dennis, G. McDonald, R. Anderson, N. Robins, and J. Close (2010), *arxiv:quant-ph/1011.5804*.
- [29] R. Folman, P. Krüger, J. Schmiedmayer, J. Denschlag, and C. Henkel, *Adv. At. Mol. Opt. Phys.* **48**, 263 (2002).
- [30] J. E. Simsarian, J. Denschlag, M. Edwards, C. W. Clark, L. Deng, E. W. Hagley, K. Helmerson, S. L. Rolston, and W. D. Phillips, *Phys. Rev. Lett.* **85**, 2040 (2000).
- [31] M. Kozuma, L. Deng, E. W. Hagley, J. Wen, R. Lutwak, K. Helmerson, S. L. Rolston, and W. D. Phillips, *Phys. Rev. Lett.* **82**, 871 (1999).
- [32] Y. Torii, Y. Suzuki, M. Kozuma, T. Sugiura, T. Kuga, L. Deng, and E. W. Hagley, *Phys. Rev. A* **61**, 041602 (2000).
- [33] V. M. Perez-Garcia, H. Michinel, J. I. Cirac, M. Lewenstein, and P. Zoller, *Phys. Rev. A* **56**, 1424 (1997).
- [34] M. Edwards, L. M. DeBeer, M. Demenikov, J. Galbreath, T. J. Mahaney, B. Nelsen, and C. W. Clark, *Journal of Physics B: Atomic, Molecular and Optical Physics* **38**, 363 (2005).
- [35] Y. Castin and R. Dum, *Phys. Rev. Lett.* **77**, 5315 (1996).
- [36] Y. B. Band, M. Trippenbach, J. P. Burke, and P. S. Julienne, *Phys. Rev. Lett.* **84**, 5462 (2000).
- [37] E. Knill and R. Laflamme, *Phys. Rev. Lett.* **81**, 5672 (1998).
- [38] G. Benenti, G. Casati, and G. Strini, *Principles of Quantum Computation and Information* (World Scientific, 2007), 1st ed.